

ARTICLE

Open Access

High-efficiency femtosecond laser fabrication of graphene-hybrid planar micro-supercapacitors with micro/nanostructured electrodes

Yuyuan Zhang^{1,2}, Tingting Zou³, Haobo Jiang⁴, Xiuyan Fu⁴, Wei Xin¹✉, Yiyang Meng¹, Xilin Li⁵, Jun-Ming Cao¹, Lin Yang¹, Yuanzheng Li¹, Weizhen Liu¹✉, Dongdong Han⁵, Xing-Long Wu¹, Jianjun Yang³, Haiyang Xu¹✉ and Yichun Liu¹

Abstract

The integration of surface-regular micro/nanostructured electrodes within a limited footprint area is promising to enhance the electrochemical performance of planar micro-supercapacitors (P-MSCs), while developing simple yet efficient manufacturing methods for such electrodes remains a challenge. Here, we propose a universal strategy combining femtosecond laser plasma lithography with spatial light modulation (SLM-FPL), fabricating well-ordered sub-wavelength micro/nanostructured electrodes of interdigital P-MSCs (SEP-MSCs) on graphene oxide (GO) films. Achieving 500/50 μm finger widths/spacings and 680 nm internal grating periods, this method enables device densities >25 units inch^{-2} with processing efficiency orders of magnitude higher than conventional laser direct writing. Further performance optimizations via wettability modification, electric field engineering, and hybrid composites (GO-MXene/COF) yield outstanding specific capacitance ($\sim 41.4 \text{ F cm}^{-3}$) and cycling stability (93% retention over 5000 cycles), supporting applications in flexible sensors and compact power supplies. This SLM-FPL technology shows strong potential for high-performance, spatially efficient SEP-MSCs in next-generation integrated systems.

Introduction

The relentless drive toward characteristic scale miniaturization and heterogeneous integration in micro/nano-optoelectronic devices has necessitated breakthroughs in energy storage technology^{1–4}. Developing next-generation portable storage systems, combining high power density and energy density, is critical to overcoming the technology bottleneck⁵. Recently, planar micro-supercapacitors (P-MSCs) stand out as promising electrochemical components among emerging solutions,

which offer exceptional power performance, ultra-long cycle life, and rapid charge/discharge capabilities^{6,7}. These attributes render them ideal for micro-energy storage, smart electronics, flexible wearable applications, and so on. The electrochemical performance of P-MSCs hinges on both the intrinsic properties of electrode materials and the interfacial structural design⁸. Strategic surface micro/nanostructuring not only amplifies electrode-specific surface areas to expose abundant active sites, but also simultaneously refines charge/ion transport pathways at electrode interfaces^{9,10}. Structural optimization enhances the transport efficiency of charges and ions, reduces the internal resistance and diffusion impedance of the electrode, thereby directly enhancing device performance.

Conventional surface micro/nanostructuring includes photolithography, ion beam etching, nanoimprinting, and self-assembly, etc.¹¹. In contrast, laser processing has emerged as an alternative, offering non-contact, adaptable

Correspondence: Wei Xin (xinwei@nenu.edu.cn) or Weizhen Liu (wzliu@nenu.edu.cn) or Haiyang Xu (hyxu@nenu.edu.cn)

¹State Key Laboratory of Integrated Optoelectronics, Key Laboratory of UV-Emitting Materials and Technology of Ministry of Education, Northeast Normal University, Changchun 130024, China

²School of Science, Jilin University of Chemical Technology, Jilin 132022, China
Full list of author information is available at the end of the article
These authors contributed equally: Yuyuan Zhang, Tingting Zou

operation that combines traditional techniques in precision and versatility^{12,13}. In particular, the femtosecond laser processing exemplifies this progress. It combines the foundational benefits of laser-material interactions with unique ultrafast dynamics, enabling sub-wavelength precision, large-area patterning, and deterministic control over micro/nanostructure formation^{14–16}. Many emerging technologies based on femtosecond laser processing achieve a critical balance between processing accuracy and throughput while maintaining the flexibility essential for complex 3D architectures at scales below the optical diffraction limit^{17–19}. Such advancements position femtosecond laser processing as a competitive frontrunner in energy device manufacturing, where hierarchical structural control and scalability are paramount.

In view of this, here we developed a versatile strategy combined femtosecond laser plasma lithography with spatial light modulation (SLM-FPL) enabling high-efficiency fabrication of silicon-based P-MSC with integrated micro/nanostructured electrodes (SEP-MSC)^{20–22}.

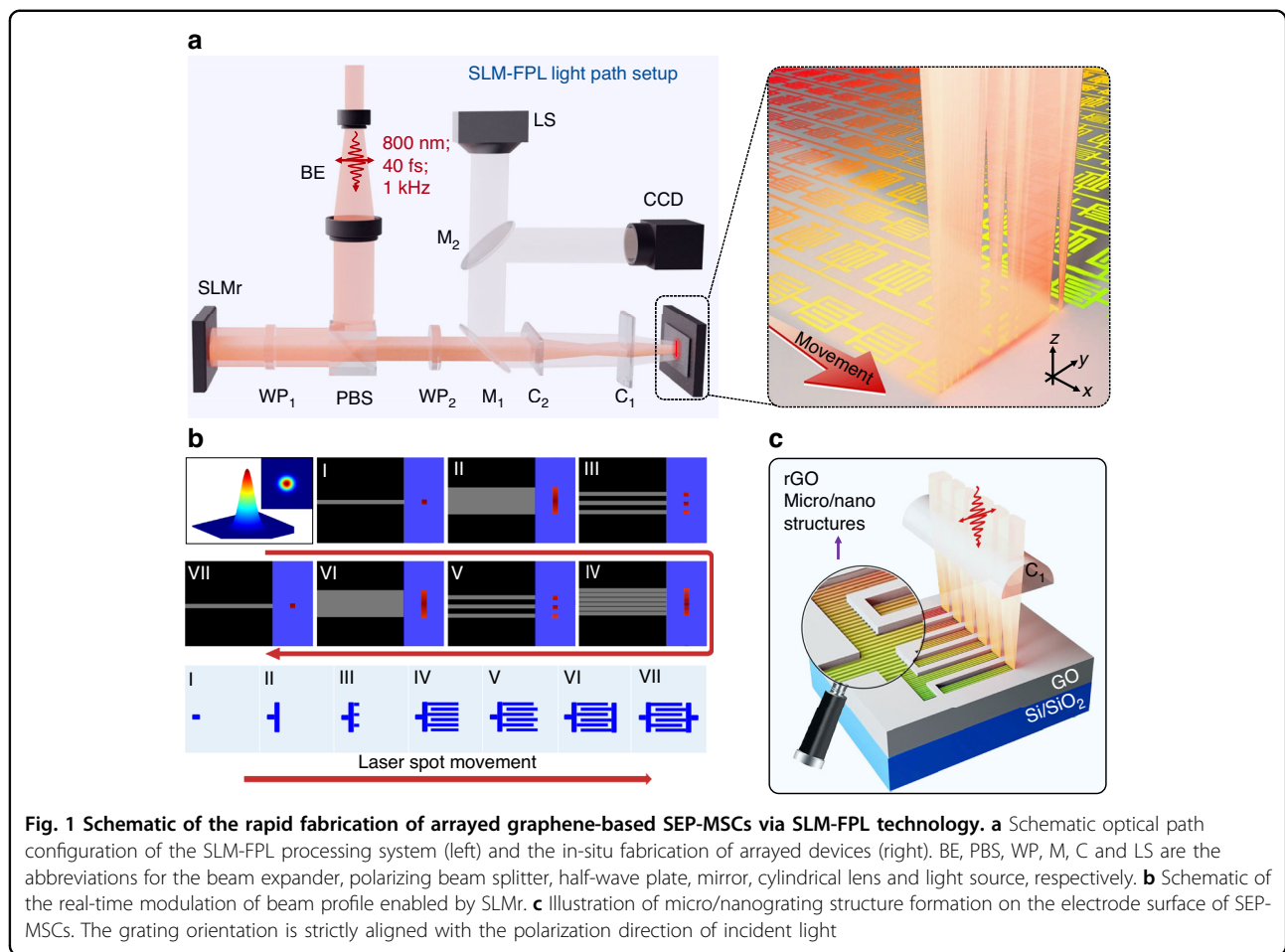
We first focused the incident femtosecond laser into a line profile on the target graphene oxide (GO) film, then employed spatial light modulator to sculpt the laser's amplitude distribution. Benefiting from the nonlinear light-matter interaction and photo-reduction capabilities inherent to FPL technology, the relative motion between the focal spot and the GO film led to the formation of reduced graphene oxide (rGO) electrodes, simultaneously patterned with large-area, well-ordered, periodic subwavelength micro/nanograting structures in the reduced regions²³. Laser parameter tuning, including wavelength, power, and scanning speed, enabled precise modulation of electrode surface morphology and GO reduction degree. Remarkably, under a scanning speed of 0.1 mm s^{-1} , micro/nanograting was performed on the interdigital electrode region with a footprint of $0.5 \times 0.5 \text{ cm}^2$ of a standard device, requiring $\sim 50 \text{ s}$ of processing time. This resulted in the formation of about 7350 laser-induced periodic surface structures (LIPSSs) with spatial period of $\sim 680 \text{ nm}$, demonstrating exceptionally high patterning density and subwavelength-scale fabrication accuracy. That means, under identical laser parameters, this strategy delivers a processing efficiency exceeding 7000-fold compared to conventional direct writing methods. Subsequent wettability measurements and numerical simulations revealed that the structures not only significantly improved surface charge transport properties but also locally enhanced the electric field intensity, thereby contributing to enhanced device performance. The volumetric capacitance of the optimized MSCs was increased by ~ 4.3 times ($\sim 23.7 \text{ F cm}^{-3}$) compared to the unstructured devices. To verify universality of the processing technology, similar experiments were further conducted on GO-MXene and GO-covalent organic framework

(COF) composite films, where material hybridization enhanced the capacitive behavior of the electrodes, leading to an additional ~ 2 -fold improvement in volumetric capacitance^{24,25}. The resulting devices exhibited excellent energy density (2.81 mWh cm^{-3}) and power density ($\sim 0.32 \text{ W cm}^{-3}$). The processing stability and regular surface micro/nanostructures enable exceptional performance uniformity and operational stability, retaining $>93\%$ electrochemical performance after 5000 charge-discharge cycles. These performance, coupled with applicability in powering compact circuits and miniaturized sensor systems, underscore the technology's potential for scalable manufacturing of high-performance SEP-MSC. The work offers further validation for the credibility of the proposed theoretical model concerning FPL processing, along with demonstrating the widespread applicability of the technology^{20,23}. Specifically, by emphasizing enhancements in capacitor performance and prioritizing high-quality fabrication, the work transcends mere technological accumulation.

Results

Ultrafast Fabrication of SEP-MSC with SLM-FPL technology

Figure 1a presents a schematic of laser processing setup based on the SLM-FPL technology^{20,21}. A femtosecond laser system operates at a central wavelength of 800 nm, with a repetition rate of 1 kHz and a pulse duration of 40 fs. The laser beam with a vertical linear polarization first passes through an expander and polarizing beam splitter (PBS) to uniformly irradiate the aperture of a spatial light modulator (SLMr). Along the reflected beam path, a half-wave plate (WP_1) rotates the polarization to horizontal for propagation toward the fabrication plane. A second half-wave plate (WP_2) is then employed to precisely adjust the laser polarization state^{20,23}. Concurrently, a pair of orthogonally arranged cylindrical lenses (CL_1 and CL_2) performs beam shaping by compressing the Gaussian profile into a linear distribution. The spatially modulated laser beam is then uniformly focused onto a silicon-supported GO film. With synchronized stage movement, large-area, arrayed graphene SEP-MSCs in series or parallel configurations can be fabricated in situ (Fig. 1a right). Following parameter optimization, here the fabrication achieves a 0.1 mm s^{-1} processing speed within a limited $0.5 \times 0.5 \text{ cm}^2$ footprint area of a standard device with interdigital electrodes featuring periodic grating structures of 680 nm. That means the configuration enables a 7000-fold enhancement in processing efficiency under identical operational conditions compared to conventional direct writing methods. For details, see the Materials and Methods section and Supplementary Information SI S1. The entire processing is monitored in real time through a coaxial charge-coupled device (CCD) imaging system.

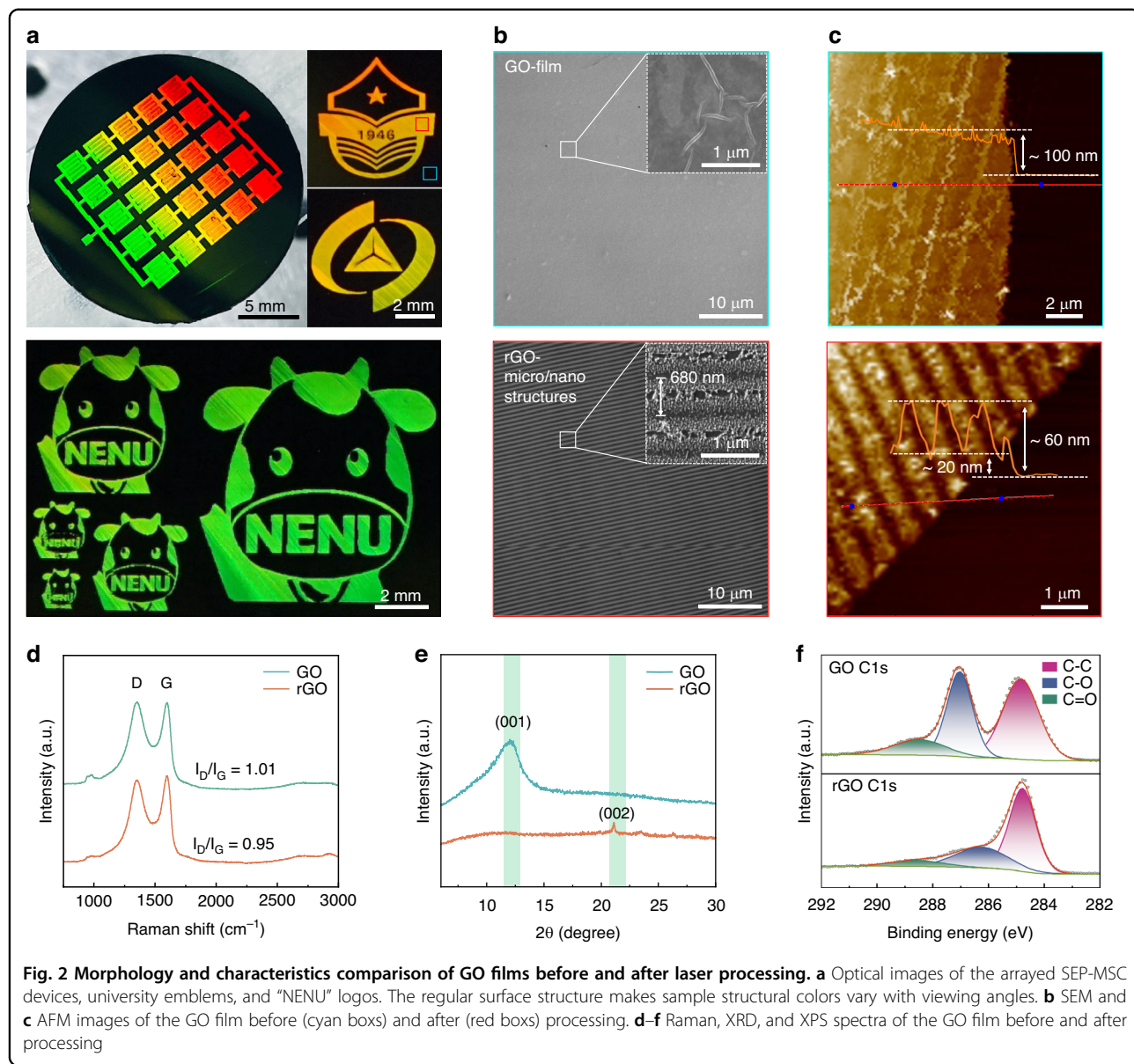


Notably, the fabrication of above graphene-based SEP-MSC device relies on the synergistic integration of multiple physical mechanisms. First, the photothermal and photochemical effects drive the reduction of GO to its reduced counterparts in laser-irradiated regions. The effective removal of oxygen-containing functional groups (OFGs) creates conductive electrodes in the device, while the unirradiated areas act as charge-blocking separators due to their insulating nature²⁶. Second, spatial beam shaping is achieved through dynamic modulation of a commercial SLMr. By precisely controlling the voltage of individual liquid crystal pixels, the grayscale reflection profile of the beam can be dynamically modulated, enabling real-time spatial amplitude shaping of the reflected laser and defining the electrode pattern in the SEP-MSC (see Fig. 1b and Methods)²¹. Finally, the ultrashort pulse duration of the femtosecond laser enables strong nonlinear optical interactions. The laser excites surface plasmon polaritons (SPPs) that interfere with the incident wave, transforming homogeneous irradiation into periodic intensity modulations (Fig. 1c). This creates sub-wavelength grating structures with tunable

orientation, periodicity, and aspect ratio, controlled by laser parameters such as polarization, wavelength, power, and repetition rate^{20,27}. The cumulative effect of these processes enables efficient, controllable, and rapid fabrication of micro/nanostructured graphene-based SEP-MSC devices. Detailed processing visualization is available in Supplementary Movies S1–4 and the Methods section.

Surface structuring and photo-reduction of GO films

We first spin-coated the GO dispersion solution onto the surface of a commercial silicon wafer, and achieved precise control over the thickness and uniformity of the film by adjusting parameters such as the number of solution droplet applications, spin-coating speed, and duration (See the Methods section and Supplementary Fig. S2 for details). Subsequently, using the aforementioned SLM-FPL technology, we performed the in-situ synchronous surface micro/nanostructuring and photo-reduction of the silicon-based GO film. Thanks to the editable regulation of the spatial amplitude distribution of the incident light spot by SLMr, the patterned processing on the GO surface exhibited high flexibility. Figure 2a



presents the arrayed series-connected SEP-MSCs fabricated by this method, as well as representative badges such as the university emblem and the “cow” logos with different sizes. It is worth noting that due to the existence of periodic micro/nanograting structures on the surface of the processed regions, the optical diffraction phenomenon is obvious and highly dependent on the observation angle. The uniform structural colors macroscopically exhibited by these patterns also reflect the high regularity, periodicity and consistency of the processed surface micro/nanostructures²⁸. To further validate the formation mechanism of the structures, comparative morphological analysis was performed on the untreated and laser-processed regions using scanning electron microscopy (SEM) and atomic force microscopy (AFM). Untreated

areas exhibited smooth, uniform surfaces with consistent material thickness (~100 nm). In contrast, laser-irradiated regions displayed well-defined periodic micro/nanograting structures characterized by ~680 nm periodicity, duty ratio of ~2:1, and etching depth of ~40 nm (Fig. 2b, c). The overall film thickness also decreased by ~40 nm post-processing. More details about the laser processing can be seen in Supplementary Fig. S3.

The observed reduction in film thickness commonly correlates with the photothermal removal of OFGs during laser-induced rGO formation^{20,29}. To validate the mechanism, we comprehensively characterized the chemical composition and crystal structure of the samples before and after laser processing by using Raman spectroscopy, X-ray diffraction (XRD), and X-ray

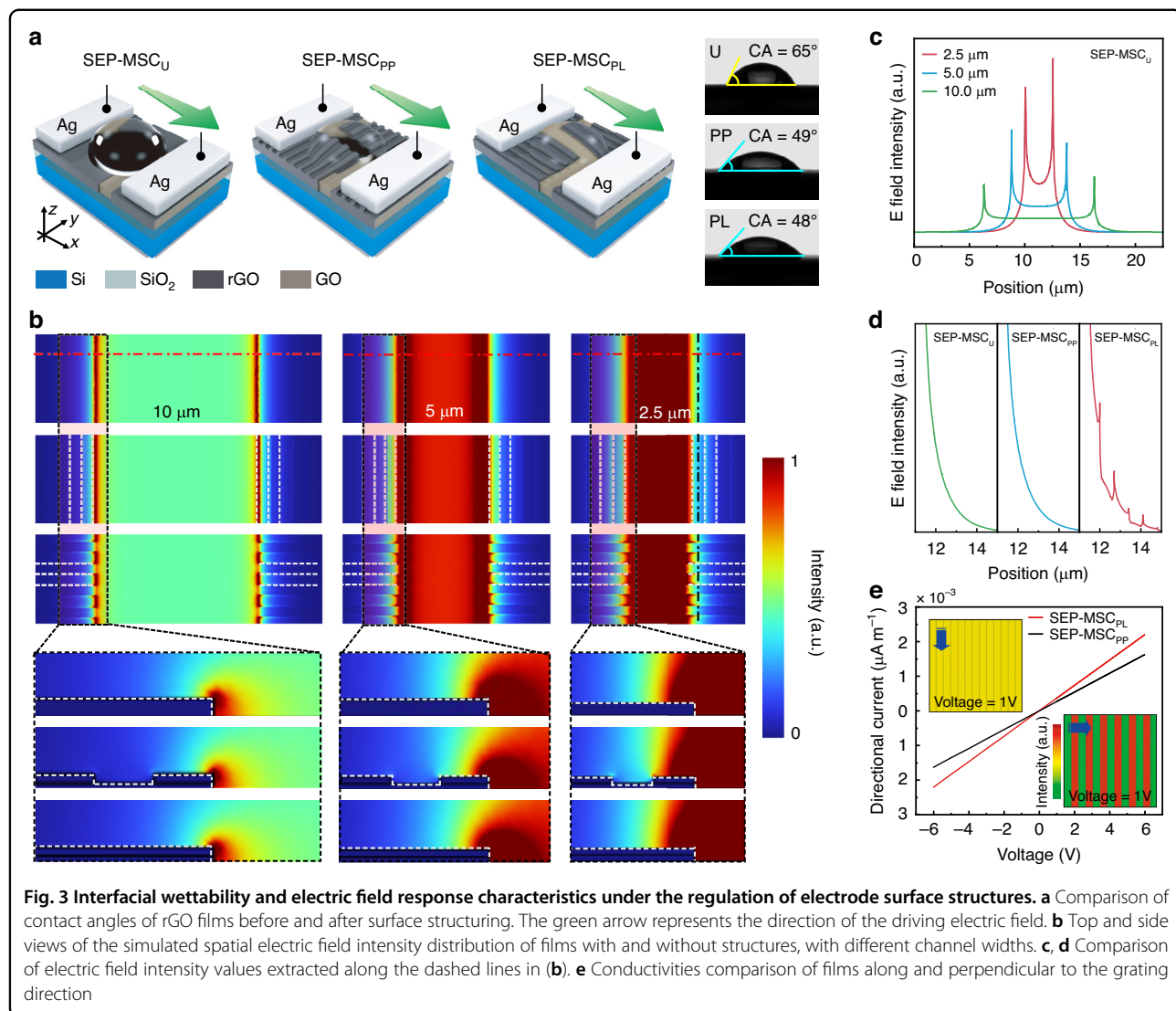
photoelectron spectroscopy (XPS). Raman analysis revealed a slight decrease in the D-to-G peak intensity ratio (I_D/I_G) from 1.01 to 0.95 post-processing (Fig. 2d), indicating partial restoration of sp^2 C-C bonds and an increased degree of graphitization³⁰. This change is a typical signature of the conversion from GO to rGO under laser irradiation. Large-scale Raman mapping scans demonstrated that the relative standard deviation (RSD) of these ratio values remained below 1.3%, underscoring the stability and uniformity of the photo-reduction (Supplementary Fig. S4). Further XRD analysis showed significant attenuation of the characteristic GO diffraction peak at $2\theta \approx 10.4^\circ$, which corresponds to its highly oxidized layered structure³¹. Another new diffraction peak at $2\theta \approx 21^\circ$ emerged, confirming more ordered rGO formations after laser processing (Fig. 2e)³². Moreover, the reduction behavior is also strongly supported by XPS analysis. In the high-resolution C 1s spectrum of the untreated GO film, characteristic peaks corresponding to C-C, C-O, and C=O bonds were observed at 284.8 eV, 287.0 eV, and 288.4 eV, respectively, with relative contents of 49.3%, 36.8%, and 13.8%. After irradiation, the relative contents of C-O and C=O functional groups decreased to 30.1% and 8.6%, respectively, indicating a significant reduction in OFGs (Fig. 2f)³³. For more details on the XPS analysis of the GO films before and after laser processing, please refer to the Supplementary Fig. S4.

Structured electrodes influence on the electrochemical performance of SEP-MSCs

The SLM-FPL technology mentioned above was subsequently employed for the in-situ rapid fabrication of interdigital rGO-based SEP-MSCs. Notably, the micro/nanograting structures introduced onto the electrode surface play a pivotal role in enhancing device electrochemical performance. On one hand, the structures significantly increased the electrode's specific surface area, thereby providing more electrochemically active sites that improve charge storage efficiency^{9,10}. The uniformity of structural dimensions ensured the stability of device performance. On the other hand, the laser-reduced rGO retained partial hydrophilic functional groups (e.g., -OH and -COOH), which could form stable hydrogen bonds with water molecules, endowing the material with excellent wettability³⁴. The laser-processed composite structure's micrometer-scale surface features also enhance hydrophilicity through capillary action³⁵. To verify this, contact angle measurements were performed using deionized water dropped onto the structured and unstructured rGO films (Fig. 3a). The unstructured rGO film exhibited a contact angle of $\sim 65^\circ$, while the rGO film with structures showed a reduced angle, decreasing by $\sim 16^\circ$, indicating improved wettability. This enhanced surface hydrophilicity facilitates closer electrode-electrolyte

contact in SEP-MSCs, promoting efficient ion transport within electrode channels, increasing active site utilization, and ultimately improving rate performance^{9,10}. Detailed wettability analysis of rGO films and their hybrids is provided in Supplementary Fig. S5.

Moreover, to investigate the impact of surface structuring on electrochemical performance, finite element method (FEM) simulations were conducted to analyze spatial electric field distributions in comparative devices with three different electrode configurations: unstructured device with smooth electrodes (SEP-MSC_U), device with grating-structured electrodes aligned parallel to the external electric field (SEP-MSC_{PL}), and devices with gratings perpendicular to the field (SEP-MSC_{PP}) (Fig. 3b, and Methods)³⁶. Among the different devices, the spacing between the electrodes was set to 2.5 μm , 5 μm , and 10 μm , respectively. The subsequent simulations revealed two critical phenomena. First, regardless of surface structuring, significant electric field enhancement occurred at electrode edges, with grating structures further amplifying this edge-field intensity, which shows a direct correlate of improved electrochemical performance (Fig. 3b, c). Second, electrode spacing exhibited an inverse relationship with edge-field strength. The shorter inter-electrode distances yielded stronger localized electric fields (Fig. 3b–d, Supplementary Fig. S6). These findings demonstrate that the surface micro/nanostructures can modulate electric field distributions, enhancing charge accumulation and ion transport at the electrode-electrolyte interface^{23,36}. Furthermore, the grating structures inherently confer conductive anisotropy to the rGO material, with charge transport properties exhibiting directional dependence^{20,23}. When charge carriers propagate parallel to the grating orientation, surface defects exert minimal interference on conductive channel conductivity, yielding superior conduction performance. Conversely, vertical charge transport suffers from interfacial scattering and structural discontinuities that suppress conductivity. The Finite element simulations quantitatively demonstrate this anisotropy under an applied voltage. The parallel-direction integrated volumetric charge density exceeds the vertical counterparts by $\sim 35\%$, yielding a ratio of 1.35, primarily due to enhanced boundary scattering and energy barrier effects in the perpendicular orientation that disrupt continuous charge pathways (Fig. 3e). The anisotropic behavior closely matches experimental observations, and the directional conductivity disparity directly impacts the electrode-electrolyte interaction (Supplementary Fig. S7). Parallel alignment between grating structures and charge transport paths maximizes electrode-electrolyte interface contact area, shortens ionic adsorption/diffusion pathways, and reduces interfacial resistance, thus favoring overall device electrochemical performance. In contrast,

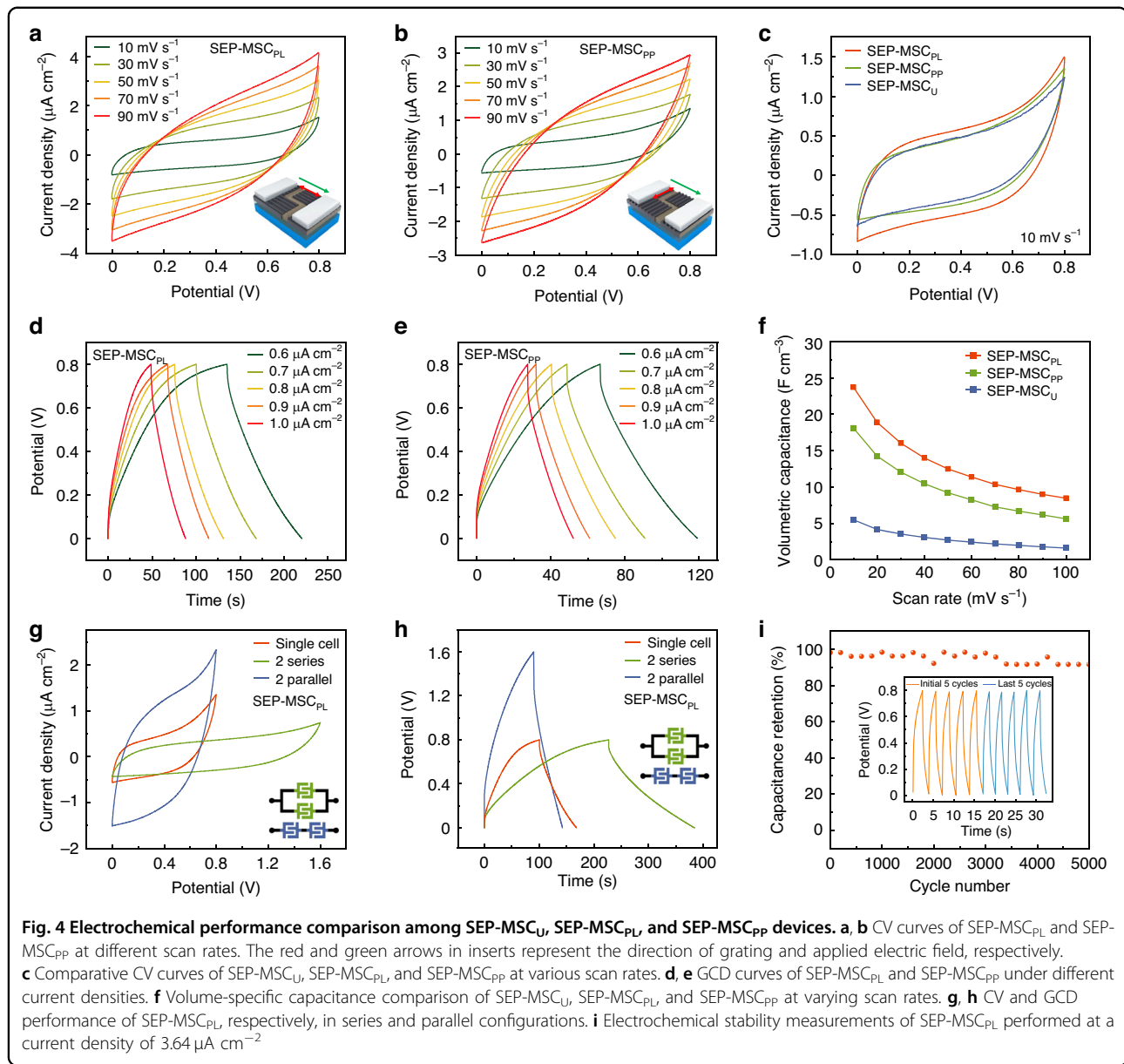


perpendicular orientation degrades interface compatibility, impedes ion migration, and compromises device functionality³⁶.

It bears noting that while above studies have demonstrated that laser-treated devices exhibit enhanced performance in terms of material wettability, local electric field enhancement, and anisotropic carrier transport, establishing a rigorous quantitative relationship between these factors with device performance proves challenging. This difficulty arises because the performance improvement stems from the synergistic interplay of multiple factors. Experimentally, when we adjust a specific parameter via laser control, other material properties also undergo alterations. Nonetheless, these findings have laid a theoretical framework for optimizing MSC performance through structured electrode design and have illuminated the path toward precisely modulating interface electric fields and ion transport dynamics.

Electrochemical performance of rGO-based SEP-MSCs

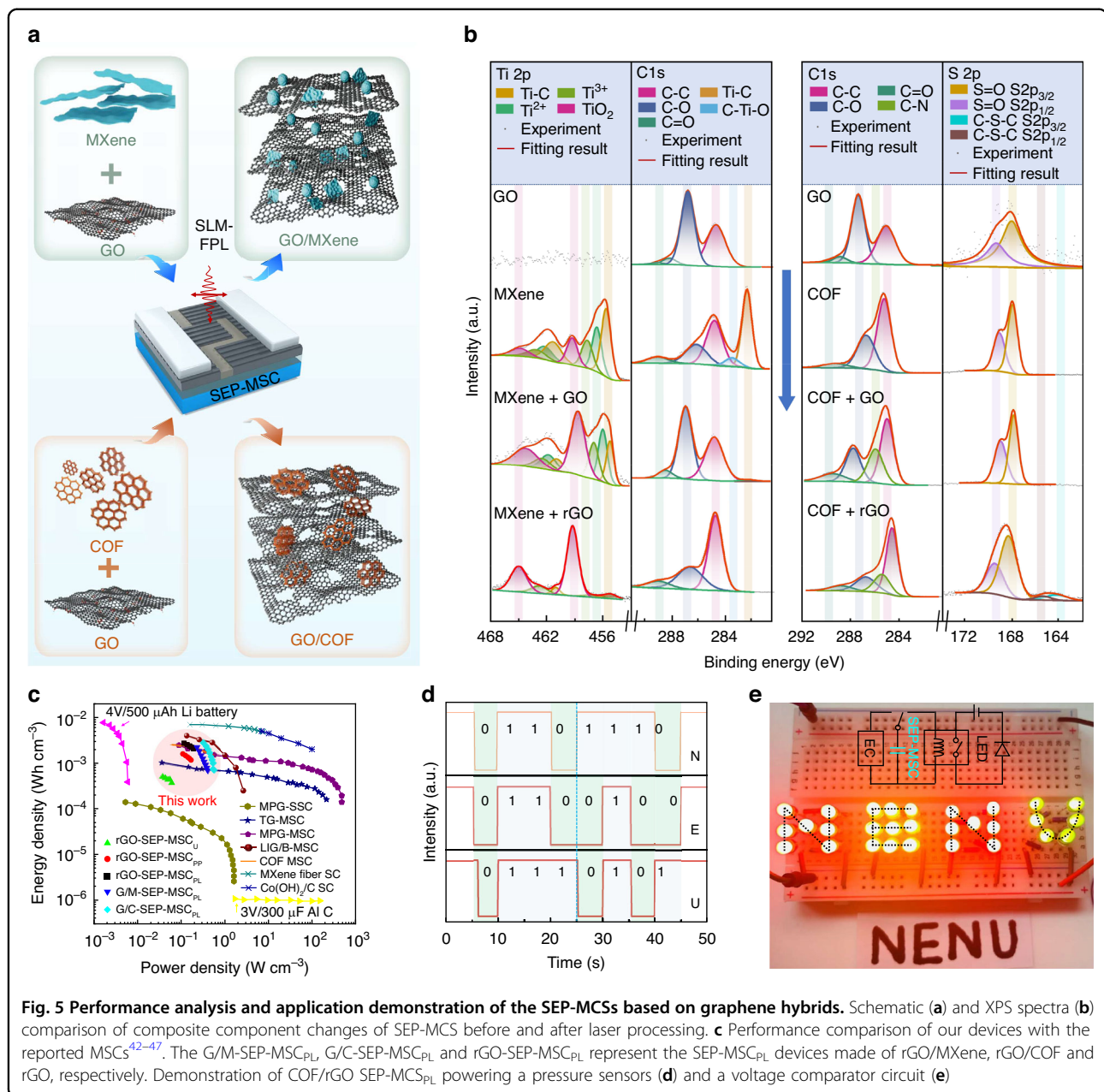
Following the mechanistic elucidation of electrodes with structures impact on the device electrochemical performance, we then fabricated the SEP-MSC_U, SEP-MSC_{PL}, SEP-MSC_{PP} with identical channel spacing of 50 μm and evaluated the performance experimentally. Figure 4a, b shows the cyclic voltammetry (CV) curves of SEP-MSC_{PL} and SEP-MSC_{PP} devices across scan rates from 10 to 90 mV s^{-1} , while Fig. 4c compares all the devices at 10 mV s^{-1} . All devices exhibited typical rectangular curves characteristic of electric double-layer capacitance, but SEP-MSC_{PL} demonstrated superior performance with the largest enclosed CV area and highest current response, indicating optimal capacitance storage capacity³⁷. The CV and galvanostatic charge-discharge (GCD) curve of the contrastive SEP-MSC_U is provided in Supplementary Fig. S8. Furthermore, GCD measurements also confirmed these findings through symmetrical



discharge profiles (Fig. 4d, e). Notably, SEP-MSC_{PL} maintained performance superiority across multiple testing parameters. Quantitative analysis of volumetric specific capacitance derived from CV data in Fig. 4f revealed that SEP-MSC_{PL} consistently achieved the highest capacitance values. At a scan rate of 10 mV s^{-1} , SEP-MSC_{PL} achieves a volumetric capacitance of 23.7 F cm^{-3} , which is 4.3 times higher than that of SEP-MSC_U. This aligns well with our previous analysis showing that micro/nanograting-induced electric field modulation at the electrode interface enhances ion transport efficiency.

Building on the processing versatility of SLM-FPL technology, we further developed the integrated device arrays using SEP-MSC_{PL} units with superior performance

as building blocks and conducted systematic electrochemical characterization. Two representative series and parallel configurations were selected for detailed analysis. Electrochemical measurements revealed that the parallel integration significantly enhanced the total capacitance, while the series arrangement effectively expanded the operating voltage window of the device ensemble (Fig. 4g, h). Notably, all the configurations maintained stable during prolonged cycling. A single SEP-MSC_{PL} unit demonstrated exceptional durability, retaining over 93% of its initial capacitance after 5000 galvanostatic charge-discharge cycles (Fig. 4i). These findings validate the technological compatibility and performance reliability of SLM-FPL in fabricating SEP-MSC devices, offering a



practical and scalable route toward highly integrated and durable on-chip energy storage units.

Performance optimization and application demonstration of GO-composite-based SEP-MSCs

To further optimize the electrochemical performance of our SEP-MSC devices, we developed composite electrodes by integrating GO respectively with advanced inorganic $Ti_3C_2T_x$ MXene and covalent organic framework (COF) nanosheets, both renowned for their exceptional capacitive properties^{24,25}. These hybrid materials were also patterned into interdigitated SEP-

MSC_{PL} devices via the SLM-FPL technology (Fig. 5a and Supplementary Fig. S9). Periodic micro/nanograting structures with well-defined orders were successfully fabricated on composite electrodes. The 2D fast Fourier transform (2D-FFT) spectra show the periods are respectively 680 ± 6.8 nm and 680 ± 4.5 nm, indicating good uniformity of gratings over a large area. Then, XPS characterization was used to reveal the structural transformations induced by laser processing. For the GO-MXene composite, post-laser treatment significantly reduced Ti-C bonds, Ti^{3+}/Ti^{2+} species, and oxygen-containing C-O/C=O groups, while concurrently

enhancing Ti-O bonds ($2p_{3/2}/2p_{1/2}$, $\sim 459.3/461.1$ eV) and C-C components. This transformation indicates the formation of a carbon-dominated hybrid conductive network with oxidized TiO_2 phases, which introduces abundant pseudocapacitive active sites (Fig. 5b left)^{38,39}. In contrast, GO-COF composites retained characteristic COF features post-processing, including C-N (~ 285.6 eV), S=O ($\sim 168.42/169.6$ eV), and C-S-C ($\sim 164.2/165.44$ eV) bonds, while increasing C-C proportions (Fig. 5b right). This suggests laser-induced formation of a carbon-based hybrid nano-skeletal framework interconnected with original COF moieties, where COF-derived nitrogen and sulfur atoms introduce additional electrochemical active sites and enhance charge transfer kinetics (Supplementary Fig. S10)^{40,41}. The synergistic effects of these material optimizations and structured electrode design yielded substantial performance improvements, achieving a volumetric capacitance of ~ 41.4 F cm $^{-3}$ in CV value. Ragone plot analysis (Fig. 5c) demonstrated that our device outperforms many reported MSCs, delivering an energy density of ~ 2.81 mWh cm $^{-3}$ while maintaining power density of ~ 0.32 W cm $^{-3}$ (Supplementary Fig. S11)⁴²⁻⁴⁷.

To validate the applicability of our SEP-MSCs, we designed and showcased two representative use cases. In the first scenario, a pre-charged SEP-MSC unit via electrochemical workstation was integrated with a flexible pressure sensor to establish a self-powered mechanical sensing system⁴⁸. The device supplied operating voltage to the sensor, where real-time pressure changes were reflected through output voltage modulation. Specifically, mechanical stimulation triggered a voltage defined as zero, while pressure release restored the output to the device's open-circuit voltage. To simplify data processing and improve signal recognition efficiency, the sensor's output voltage underwent normalization before analysis. Figure 5d shows the binary encoding-based pattern recognition results of the letters "N", "E" and "U" based on the mechanism, visually demonstrating the potential for flexible human-machine interfaces and information recognition systems. In the second demonstration, the SEP-MSC was employed as an independent micro-power source to drive a voltage comparator circuit, testing its capability in logic control applications⁴⁹. A test system was constructed based on the classic working model (Fig. 5e). Following stable charging, the device's output was connected to the comparator's input. When the device output reached the preset threshold voltage of 0.3 V, the comparator was activated, immediately illuminating an output-connected light-emitting diode. This rapid response confirmed the ability of our SEP-MSC device to reliably trigger low-power electronic components. A video of the experiments is provided in Supplementary Movie S5.

The above results comprehensively demonstrate the practical viability of our SEP-MSC devices for power supplies in portable electronics, flexible sensor networks, and microscale logic systems. They highlight the distinctive capabilities of our SLM-FPL technology in enabling precise fabrication and processing of SEP-MSC devices on silicon substrates, which holds significant promise for advancing on-chip intelligent sensing applications. However, current fabrication methodologies exhibit certain limitations in device manufacturing efficiency, flexibility of electrode surface micro/nano-structuring, and overall capacitance performance. These challenges present opportunities for improvement through systematic optimization. Notably, the inherent strengths of SLM-FPL technology, particularly its capacity for microscopic nonlinear light-matter interactions and macroscopic optical path control, provide a robust foundation for addressing these limitations. By refining laser processing parameters and device structural configurations, we anticipate breakthroughs in fabrication efficiency and structural adaptability. For example, emerging researches have indicated that the nonlinear mechanisms inherent to FPL technology could enable the creation of deep sub-wavelength periodic structures on 2D film surfaces⁵⁰. When combined with optimized optical path design and post-processing techniques, this capability may facilitate the fabrication of more complex multi-layer architectures⁵¹. For SEP-MSC devices, performance enhancements could also be achieved through material-level innovations, including increased energy storage material thickness, optimized composite systems, and hierarchical electrode structures⁵². Such advancements would not only elevate electrochemical performance but also broaden application scope, solidifying the technological foundation for integrated micro-power solutions in advanced sensing and portable electronics. Looking ahead, through the optimization of experimental parameters, such as augmenting laser power and scaling up the dimensions of optical components, and integrating it with complementary linkage equipment, the SLM-FPL technology is poised to transition into practical applications especially the on-chip energy systems.

Discussion

In conclusion, we have demonstrated a versatile and high-efficiency strategy for fabricating SEP-MSCs by synergizing SLM-FPL technology. Leveraging the nonlinear light-material interactions inherent to femtosecond lasers and the programmable patterning flexibility of SLMr, the method enables large-area arrayed interdigital devices fabrication on diverse materials while achieving in-situ regular sub-wavelength micro/nanograting structuring with period of ~ 680 nm within confined electrode regions. Multiple mechanisms, such as increasing

electrode-specific surface area via hierarchical structures, optimizing ion transportation through wettability modulation and localized electric field engineering, and synergistic properties from hybrid composites (GO, GO-MXene and GO-COF), have been considered during processing to enhance the device electrochemical performances. A representative implementation demonstrates exceeding 25 devices per square inch with outstanding energy density (2.81 mWh cm^{-3}), power density ($\sim 0.32 \text{ W cm}^{-3}$) and over 93% capacitance retention after 5000 cycles, validating its practical viability for flexible sensing systems and compact power modules. Our SLM-FPL technology provides a feasible platform for tailoring surface structuring functionalities and optimizing energy storage interfaces, presenting technical compatibility for the development of next-generation miniaturized energy storage devices with high integration density and reliability.

Materials and methods

Preparation of GO, GO-MXene, and GO-COF

GO dispersion (2 mg mL^{-1} , flake size 20–30 μm , Gaoxi Tech Co., Ltd) was drop-cast onto oxygen plasma-pretreated Si/SiO₂ wafers, followed by repeated casting for controlled thickness and room-temperature drying before laser processing. For MXene/GO films, Ti₃AlC₂ MAX phase was synthesized by sintering Ti, Al, and C powders (3:1:2 molar ratio) at 1650 °C under argon for 2 h, then ball-milled, sieved, and etched in 12 M LiF/9 M HCl for 24 h to remove Al. After rinsing to neutral, the product was ultrasonicated under argon in an ice bath for 20 minutes, and the supernatant (Ti₃C₂T_x) was mixed with GO at 1:12 mass ratio for homogeneous suspension before drop-casting. For COF/GO films, Tp (128 mg, 0.61 mmol) and Pa-SO₃H (172 mg, 0.92 mmol) were dissolved in 10 mL DMSO each, sonicated for 15 min, then the aldehyde solution was dropwise added to the amine solution under stirring. The mixture was kept at 60 °C for 48 h to form a COF, which was blended with GO at 1:10 mass ratio, stirred, and drop-cast following the same procedure. All the reagents and solvents used here were purchased from commercial sources and were used without further purification.

Femtosecond laser fabrication

The SEP-MSCs with large-area, well-ordered, periodic sub-wavelength micro/nanogratings on electrodes were fabricated using a commercial chirped-pulse amplification femtosecond laser system (Spitfire Ace, Spectra Physics), delivering 800 nm wavelength, 40 fs pulse duration, and a repetition rate of 1 kHz. The laser beam, modulated by a SLMr (Hamamatsu, LCOS-SLM X13138-02, Output wavelength: $800 \pm 50 \text{ nm}$; Light utilization efficiency: 97% @ 800 nm; Resolution: 1272×1024 ; Active area:

$15.9 \times 12.8 \text{ mm}$), was focused into a line-shaped spot on the film sample surface using two cylindrical lenses. The device was fabricated using a laser power maintained at 120 mW and a scanning speed set to 0.1 mm s^{-1} . Pattern generation was based on a 256×256 pixel grayscale image, enabling grayscale variation along the y-axis of the SLMr microplane. The grayscale values were used to simulate the aperture state, establishing a direct correlation between laser intensity distribution and electrode geometry. The patterning process was controlled in real time using a LabVIEW program, which synchronized SLMr modulation with three-axis stage movement to achieve precise writing of the designed structures.

Notably, the processing efficiency enhancement mentioned above refers to the ratio of fabrication throughput between FPL and conventional direct writing laser technique. Within the standard device area measuring $\sim 0.5 \times 0.5 \text{ cm}^2$, there are ~ 7350 grooves with a period of 680 nm. The grooves can be generated in a single pass of the light spot by employing FPL, whereas traditional direct writing necessitates multiple reciprocating movements of light spot to accomplish the same task. Although theoretically, enhancing the direct writing speed could boost efficiency, given factors such as sub-wavelength processing accuracy and the fragility of the film material, merely increasing the speed fails to effectively address the issue of processing throughput. More information can be seen in Supplementary Fig. S1.

Electric field characteristic simulations of the structured electrodes

The electric field characteristics of the electrodes was simulated using COMSOL Multiphysics' Electrostatics and Electric Currents modules. A realistic MSC geometry was modeled to calculate the global potential and electric field distributions, considering channel widths ranging from 2.5 μm to 250 μm . For analysis of local electric field behavior, a simplified symmetric structure with opposing electrode pairs was developed, incorporating periodic grating micro/nanostructures on the electrode surfaces. Boundary conditions were set with one electrode at 0 V and the opposite electrode at 1 V, matching experimental conditions. The electric field intensity was calculated using the standard formulation.

$$\nabla \cdot \mathbf{D} = \rho \quad (1)$$

$$\mathbf{E} = -\nabla V \quad (2)$$

Where \mathbf{D} is the electric displacement, ρ is the space charge density, \mathbf{E} is the electric field, and V is the electric potential. Electrical anisotropy of the grating structures was evaluated using COMSOL Multiphysics' Electric

Currents module for steady-state current analysis, focusing on electronic conductivity. The model incorporated periodically arranged conductive/insulating gratings with dimensional parameters matching experimental configurations. Electric field orientations were applied parallel and perpendicular to the grating direction, while other boundaries were assigned electrically insulating conditions. A pronounced conductivity contrast was defined between conductive and insulating regions. The current density vector field (\mathbf{J}) was extracted, and its component along the electric field direction was volume-integrated to quantify electrical anisotropy.

$$I_X = \int_V J_X dV \quad (3)$$

Properties and electrochemical performance

characterizations of MSCs

Optical microscopy images were acquired using a confocal laser microscope (Keyence, VK-X1000), while morphological analysis at the nanoscale was achieved via field-emission scanning electron microscopy (FE-SEM, Hitachi, SU8600). Film topography were quantified in tapping mode using an AFM (Bruker, Dimension Icon). Material composition and crystal structure were investigated through confocal Raman spectroscopy (Horiba, LabRAM HR-Evolution) using a 532 nm laser source, XPS (AXIS SUPRA+), and XRD (Rigaku D/max-2500 X-ray diffractometer). The contact angle was measured using contact angle goniometer (POWERREACH, JC2000D3) by dropping 7 μ L of deionized water.

Electrochemical performance was evaluated using a CHI 760E electrochemical workstation with silver wires employed for electrode interconnection. A solid-state H_3PO_4 -PVA gel electrolyte was deposited onto the electrode active regions. The electrolyte was prepared by dissolving 6 g of H_3PO_4 in 60 mL deionized water, followed by gradual addition of 6 g PVA powder under continuous stirring. The mixture was heated to 85 °C and maintained under vigorous agitation until a transparent gel formed, then allowed to cool to room temperature under ambient ventilation prior to application.

Based on the CV curves, the areal capacitance (C_A , in F cm^{-2}) was calculated using the following equation.

$$C_A = \frac{1}{S \times \nu \times \Delta V} \int_{V_i}^{V_f} I(V) dV \quad (4)$$

Where S is the area of the active electrode (cm^2), ΔV is the voltage window (V), ν is the scan rate (V s^{-1}), and V_f and V_i are the upper and lower voltage limits of the CV curve, respectively. $I(V)$ represents the current in amperes at a given voltage, and the integral $\int_{V_i}^{V_f} I(V) dV$ corresponds to

the enclosed area under the CV curve. The C_A at different current densities was further calculated from the GCD curves using the corresponding formula.

$$C_A = \frac{1}{S \times (dV/dt)} \quad (5)$$

Where I is the discharge current (A), and dV/dt is the voltage change rate of the constant-current discharge curve. The C_V was calculated using the following formula.

$$C_V = \frac{C_A}{d} \quad (6)$$

Where d denotes the effective thickness of the electrode. The volumetric energy density (E_V , Wh m^{-3}) is calculated using the following equation:

$$E_V = \frac{1}{2} \times C_A \times \frac{(\Delta V)^2}{3600} \quad (7)$$

Where $\Delta V = V_{\max} - V_{\text{drop}}$ represents the discharge voltage window (V). The V_{\max} is the maximum voltage and V_{drop} is the initial voltage drop at the beginning of the discharge plateau, representing the voltage drop phenomenon. The volumetric power density (P_V , W cm^{-3}).

$$P_V = \frac{E_V}{\Delta t} \times 3600 \quad (8)$$

Where Δt represents the discharge time (S).

Acknowledgements

This work was supported financially by the National Natural Science Foundation of China (NSFC) (52025022, 12274065, 22478149, 12474421, 62505109, 12204477, 52302166, 62275045, 62574038); Fund from Jilin Province (20260601020RC); Hong Kong Scholar Program (XJ2024039), Hong Kong, China; "111 Center" (B25030); and the Fundamental Research Funds for the Central Universities (No. 2412025PD013).

Author details

¹State Key Laboratory of Integrated Optoelectronics, Key Laboratory of UV-Emitting Materials and Technology of Ministry of Education, Northeast Normal University, Changchun 130024, China. ²School of Science, Jilin University of Chemical Technology, Jilin 132022, China. ³GPL Photon Lab, State Key Laboratory of Luminescence Science and Technology, Changchun Institute of Optics, Fine Mechanics and Physics, Chinese Academy of Sciences, Changchun 130033, China. ⁴Key Laboratory of Functional Materials Physics and Chemistry of Ministry of Education, Jilin Normal University, Changchun 130103, China. ⁵State Key Laboratory of Integrated Optoelectronics, JLU Region, College of Electronic Science and Engineering, Jilin University, Changchun 130012, China

Author contributions

W.X., W.Z.L. and H.Y.X. proposed the research concept and designed the experiments. The experiments for material preparation, as well as morphology and composition characterization, were carried out by Y.Y.Z. with the assistance of H.B.J., X.Y.F. and Y.Y.M. The construction of the optical path and laser processing were performed by T.T.Z. and J.J.Y. The numerical simulation of electric field distribution and the wettability characterization of the material were conducted by Y.Y.Z. The electrochemical characterizations and other application experiments were carried out by X.L.L., J.M.C., L.Y. and X.L.W. All authors

participated in the discussion and analysis of the results. The manuscript was collaboratively written by W.X., Y.Z.L. and D.D.H. H.Y.X., W.X., W.Z.L., Y.Z.L., J.M.C., L.Y. and T.T.Z. provided support and supervision for the project.

Data availability

All data are available in the main text or the supplementary materials. Additional data supporting the findings of this study are available from the corresponding author upon reasonable request.

Conflict of interest

The authors declare no competing interests.

Supplementary information The online version contains supplementary material available at <https://doi.org/10.1038/s41377-025-02182-5>.

Received: 29 September 2025 Revised: 18 December 2025 Accepted: 28 December 2025

Published online: 21 January 2026

References

1. Zhang, P. P. et al. Two-dimensional materials for miniaturized energy storage devices: from individual devices to smart integrated systems. *Chem. Soc. Rev.* **47**, 7426–7451 (2018).
2. Kyeremateng, N. A., Brousse, T. & Pech, D. Microsupercapacitors as miniaturized energy-storage components for on-chip electronics. *Nat. Nanotechnol.* **12**, 7–15 (2017).
3. Wu, N. F. et al. Intelligent nanophotonics: when machine learning sheds light. *eLight* **5**, 5 (2025).
4. Yao, J. et al. Nonlocal Huygens' meta-lens for high-quality-factor spin-multiplexing imaging. *Light Sci. Appl.* **14**, 65 (2025).
5. Lethien, C., Le Bideau, J. & Brousse, T. Challenges and prospects of 3D micro-supercapacitors for powering the internet of things. *Energy Environ. Sci.* **12**, 96–115 (2019).
6. Gao, W. et al. Direct laser writing of micro-supercapacitors on hydrated graphite oxide films. *Nat. Nanotechnol.* **6**, 496–500 (2011).
7. Xiao, H. et al. One-step device fabrication of phosphorene and graphene interdigital micro-supercapacitors with high energy density. *ACS Nano* **11**, 7284–7292 (2017).
8. El-Kady, M. F. et al. Engineering three-dimensional hybrid supercapacitors and microsupercapacitors for high-performance integrated energy storage. *Proc. Natl. Acad. Sci. USA* **112**, 4233–4238 (2015).
9. Wang, Y. et al. Fixture-free omnidirectional prestretching fabrication and integration of crumpled in-plane micro-supercapacitors. *Science Adv.* **8**, eabn8338 (2022).
10. Wang, T. et al. Machine-learning-assisted material discovery of oxygen-rich highly porous carbon active materials for aqueous supercapacitors. *Nat. Commun.* **14**, 4607 (2023).
11. Lv, H. Z. et al. A review on nano-/microstructured materials constructed by electrochemical technologies for supercapacitors. *Nano Micro Lett.* **12**, 118 (2020).
12. Kumar, R. et al. Laser processing of graphene and related materials for energy storage: state of the art and future prospects. *Prog. Energy Combust. Sci.* **91**, 100981 (2022).
13. Wang, H. M. et al. Laser-processed functional surface structures for multi-functional applications-a review. *J. Manuf. Process.* **116**, 247–283 (2024).
14. Wang, X. J. et al. Laser manufacturing of spatial resolution approaching quantum limit. *Light Sci. Appl.* **13**, 6 (2024).
15. Guan, Y. C. et al. Far-field femtosecond laser-driven $\lambda/73$ super-resolution fabrication of 2D van der Waals NbO₂ nanostructures in ambient air. *Nat. Commun.* **16**, 4149 (2025).
16. Khurjin, J., Bykov, A. Y. & Zayats, A. V. Hot-electron dynamics in plasmonic nanostructures: fundamentals, applications and overlooked aspects. *eLight* **4**, 15 (2024).
17. Liu, H. G., Lin, W. X. & Hong, M. H. Hybrid laser precision engineering of transparent hard materials: challenges, solutions and applications. *Light Sci. Appl.* **10**, 162 (2021).
18. Saha, S. K. et al. Scalable submicrometer additive manufacturing. *Science* **366**, 105–109 (2019).
19. Miyaji, G. A. et al. Stable fabrication of femtosecond-laser-induced periodic nanostructures on glass using real-time monitoring and active feedback control. *Light Adv. Manuf.* **6**, 7 (2025).
20. Zou, T. T. et al. High-speed femtosecond laser plasmonic lithography and reduction of graphene oxide for anisotropic photoresponse. *Light Sci. Appl.* **9**, 69 (2020).
21. Yuan, Y. J. et al. Laser photonic-reduction stamping for graphene-based micro-supercapacitors ultrafast fabrication. *Nat. Commun.* **11**, 6185 (2020).
22. Liu, X. et al. Laser-scribed graphene for sensors: preparation, modification, applications, and future prospects. *Light Adv. Manuf.* **4**, 14 (2023).
23. Zou, T. T. et al. Birefringent response of graphene oxide film structurized via femtosecond laser. *Nano Res.* **15**, 4490–4499 (2022).
24. Li, X. L. et al. MXene chemistry, electrochemistry and energy storage applications. *Nat. Rev. Chem.* **6**, 389–404 (2022).
25. Huang, T. et al. Single solution-phase synthesis of charged covalent organic framework nanosheets with high volume yield. *Angew. Chem. Int. Ed.* **62**, e20209306 (2023).
26. Wang, S. et al. Scalable fabrication of photochemically reduced graphene-based monolithic micro-supercapacitors with superior energy and power densities. *ACS Nano* **11**, 4283–4291 (2017).
27. Bonse, J. et al. Laser-induced periodic surface structures—a scientific evergreen. *IEEE J. Sel. Top. Quantum Electron.* **23**, 9000615 (2017).
28. Li, Y. H. et al. Vivid structural color macropatterns created by flexible nanopainting of ultrafast lasers. *ACS Appl. Mater. Interfaces* **14**, 21758–21767 (2022).
29. Zhang, Y. L. et al. Direct imprinting of microcircuits on graphene oxides film by femtosecond laser reduction. *Nano Today* **5**, 15–20 (2010).
30. Lin, J. et al. Laser-induced porous graphene films from commercial polymers. *Nat. Commun.* **5**, 5714 (2014).
31. Krishnamoorthy, K. et al. The chemical and structural analysis of graphene oxide with different degrees of oxidation. *Carbon* **53**, 38–49 (2013).
32. Liu, Z. et al. Oxygen clusters distributed in graphene with "paddy land" structure: ultrahigh capacitance and rate performance for supercapacitors. *Adv. Funct. Mater.* **28**, 1705258 (2018).
33. Fatkullin, M. et al. Photochemistry dominates over photothermal effects in the laser-induced reduction of graphene oxide by visible light. *Nat. Commun.* **15**, 9711 (2024).
34. Mouhat, F., Coudert, F. X. & Bocquet, M. L. Structure and chemistry of graphene oxide in liquid water from first principles. *Nat. Commun.* **11**, 1566 (2020).
35. Samanta, A. et al. Roles of chemistry modification for laser textured metal alloys to achieve extreme surface wetting behaviors. *Mater. Des.* **192**, 108744 (2020).
36. Yuan, Y. J. et al. Laser maskless fast patterning for multitype micro-supercapacitors. *Nat. Commun.* **14**, 3967 (2023).
37. Balasubramaniam, S. et al. Comprehensive insight into the mechanism, material selection and performance evaluation of supercapacitors. *Nano Micro Lett.* **12**, 85 (2020).
38. Brette, F. et al. XPS binding energy shifts in 2D Ti₃C₂T_x MXene go largely beyond intuitive explanations: rationalization from DFT simulations and experiments. *Small Methods* **9**, 2400848 (2025).
39. Yang, Q. Y. et al. MXene/graphene hybrid fibers for high performance flexible supercapacitors. *J. Mater. Chem. A* **5**, 22113–22119 (2017).
40. Li, J. et al. Bulk COFs and COF nanosheets for electrochemical energy storage and conversion. *Chem. Soc. Rev.* **49**, 3565–3604 (2020).
41. Xia, J. et al. Electrospinning fabrication of flexible, foldable, and twistable Sb₂S₃/TiO₂/C nanofiber anode for lithium ion batteries. *Chem. Eng. J.* **413**, 127400 (2021).
42. El-Kady, M. F. & Kaner, R. B. Scalable fabrication of high-power graphene micro-supercapacitors for flexible and on-chip energy storage. *Nat. Commun.* **4**, 1475 (2013).
43. Chen, Y. J. et al. Graphene-based in-planar supercapacitors by a novel laser-scribing, in-situ reduction and transfer-printed method on flexible substrates. *J. Power Sources* **420**, 82–87 (2019).
44. Zhang, J. Z. et al. Highly conductive Ti₃C₂T_x MXene hybrid fibers for flexible and elastic fiber-shaped supercapacitors. *Small* **15**, 1804732 (2019).
45. Wang, Y. M. et al. Wood-derived hierarchically porous electrodes for high-performance all-solid-state supercapacitors. *Adv. Funct. Mater.* **28**, 1806207 (2018).
46. Peng, Z. W. et al. Flexible boron-doped laser-induced graphene micro-supercapacitors. *ACS Nano* **9**, 5868–5875 (2015).
47. Li, X. L. et al. Direct laser scribing of all-solid-state in-plane proton micro-supercapacitors on ionic covalent organic framework films. *Adv. Funct. Mater.* **35**, 2423854 (2025).

48. Qin, J. Q. et al. Hierarchical ordered dual-mesoporous polypyrrole/graphene nanosheets as bi-functional active materials for high-performance planar integrated system of micro-supercapacitor and gas sensor. *Adv. Funct. Mater.* **30**, 1909756 (2020).
49. Guo, H. et al. Femtosecond laser bessel beam fabrication of a supercapacitor with a nanoscale electrode gap for high specific volumetric capacitance. *ACS Appl. Mater. Interfaces* **14**, 39220–39229 (2022).
50. Beltaos, A. et al. Femtosecond laser induced periodic surface structures on multi-layer graphene. *J. Appl. Phys.* **116**, 204306 (2014).
51. Öktem, B. et al. Nonlinear laser lithography for indefinitely large-area nanosstructuring with femtosecond pulses. *Nat. Photonics* **7**, 897–901 (2013).
52. Yuan, Y. J. et al. Laser-induced electron synchronization excitation for photochemical synthesis and patterning graphene-based electrode. *Adv. Mater.* **36**, 2308368 (2024).